# Anomalous plasma evolution in the erosion process in high-power reactive magnetron sputtering

Cite as: Phys. Plasmas **32**, 023907 (2025); doi: 10.1063/5.0244132
Submitted: 16 October 2024 · Accepted: 31 January 2025 ·
Published Online: 26 February 2025

Suihan Cui,[1,2,a)] Dongjie Yang,[1] Shiyi Tang,[1] Ziqi Ma,[1] Mengran Xiao,[1] Xiaokai An,[1] Wei Lv,[3] Wanli Luo,[3] Qinfang Yu,[3] Liangliang Liu,[1,2] Ricky K. Y. Fu,[2] Paul. K. Chu,[2] and Zhongzhen Wu[1,a)]

## AFFILIATIONS

[1]School of Advanced Materials, Peking University Shenzhen Graduate School, 518055 Shenzhen, China
[2]Department of Physics, Department of Materials Science and Engineering, and Department of Biomedical Engineering, City University of Hong Kong, 999077 Tat Chee Avenue, Kowloon, Hong Kong, China
[3]Shenzhen Jinjia Group, 518038 Shenzhen, China

[a)]Authors to whom correspondence should be addressed: cuish@pku.edu.cn and wuzz@pku.edu.cn

## ABSTRACT

During magnetron sputtering erosion, the change in the morphology and magnetic field of the target surface affects the plasma discharge. Especially in high power and reactive conditions, the plasma evolution during erosion determines the continuity and stability of the discharge. In this work, a global model with iterative modification of the erosion profile is established, by which the reactive sputtering of an Al target in $Ar/N_2$ is simulated to study the plasma evolution and surface combination in the erosion process at different power densities. With increasing discharge power density, the electron density and electron temperature increase significantly to enhance plasma ionization. Consequently, the proportion of adsorbed $N_2$ participating in surface combination decreases from 70% to 31%, while the proportions of N deposition and N-containing ion sub-plantation increase to 44% and 25%, respectively. In the erosion process, the proportion of N participating in surface combination remains essentially unchanged at low power densities. In contrast, at a large power density, $N_2$ adsorption weakens, and the proportion of N-containing ion sub-plantation increases further from 25% to 37%, becoming the main reason for target poisoning. Calculation of the generation and consumption of target surface compounds reveals that the coverage rate of target surface compounds decreases and then increases in the sputtering process at a low power density, while that rises all the time at a large power density, leading to a severe target poisoning.

© *2025 Author(s). All article content, except where otherwise noted, is licensed under a Creative Commons Attribution (CC BY) license (https://creativecommons.org/licenses/by/4.0/).* https://doi.org/10.1063/5.0244132

## I. INTRODUCTION

Target poisoning[1] is a common phenomenon in reactive sputtering.[2] With the target erosion, significant changes in the target morphology and surface magnetic field take place,[3] consequently changing the target poisoning conditions[4] and affecting the continuity and stability of the discharge and quality of the deposited coatings. Especially under high-power reactive sputtering conditions, the discharge is often interrupted at deeper erosion stage, but it is difficult to restart under the same discharge conditions. In spite of using feedback of the discharge voltage or spectra, the control of the sputter deposition process is extremely poor.

Target poisoning in reactive magnetron sputtering is a problem of concern in the industry. Generally, it is believed that the state of target poisoning depends on the dynamic equilibrium between the formation and consumption of compounds on the target surface.[5] The former includes molecular adsorption, atom deposition, and ion sub-plantation of the reactive gas species, while the latter mainly involves ion sputtering.[6] Berg *et al.*[7] have suggested that ionization of the reactive gas can be neglected when the partial pressure of the reactive gas is much lower than that of the working gas. Based on the balance between reactive gas adsorption and ion sputtering, the Berg model is established to provide a quantitative description of the target poisoning state.[7–10] Güttler *et al.*[11,12] have monitored the hysteresis of reactive gases *in situ* and found that the absorption of reactive gases on the cathode mainly involves molecular adsorption and atom deposition, rather than direct ion sub-plantation, further proving the basic

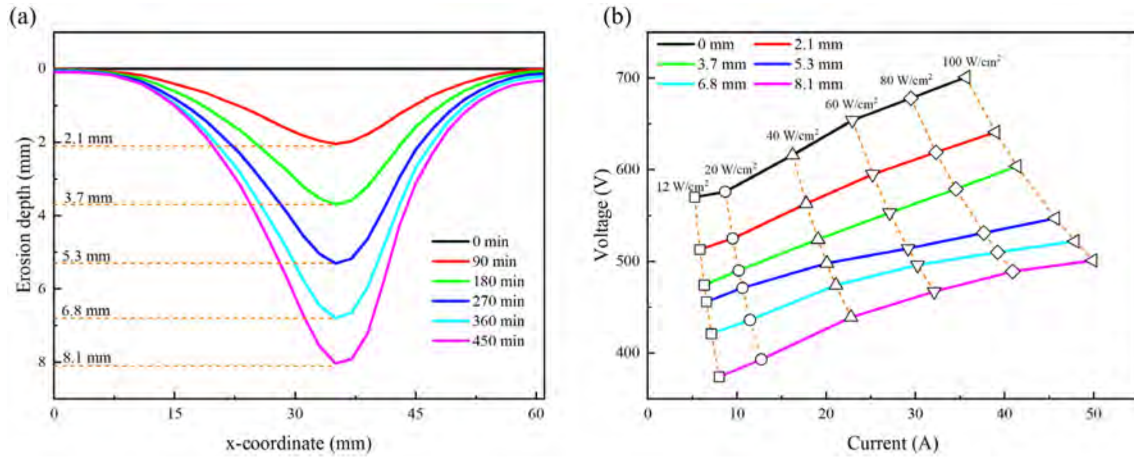


**FIG. 1.** (a) Erosion profiles after reactive sputtering for 0, 90, 180, 270, 360, and 540 min at a power density of 100 W/cm$^2$; (b) Volt-ampere characteristics measured at 12, 20, 40, 60, 80, and 100 W/cm$^2$.

assumption of the Berg model. According to the Berg model, reactive gas adsorption and atom deposition vary very little with the cathode erosion. Therefore, only the ion sputtering yield changes slightly with variations of the discharge parameters during conventional magnetron sputtering.[4] Hence, reactive sputtering is relatively stable. However, in the large power density regime, the discharge voltage and plasma density increase significantly, consequently boosting the ionization rate and energy of the reactive particles in the plasma.[13] As a result, the instantaneous erosion rate increases rapidly, resulting in a faster morphological variation of the target surface.[3] Meanwhile, the reactivity of reactive ions is high, thus enabling more reactive ions to participate in compound formation and sputtering of the target surface. In this case, the evolution of the target surface morphology and discharge parameters during erosion become the determining factors of the plasma discharge and target surface combination, thereby affecting the continuity and stability of the reactive ion discharge.

Herein, using the reactive sputtering of an Al target in the Ar/$N_2$ atmosphere as an example, we establish a global model with iterative modification of the erosion profile to describe the reactive sputtering process. The plasma evolution and target surface combination during reactive ion sputtering are studied by the model. Owing to the significantly enhanced plasma ionization at a large power density, more reactive ions participate in the combination process on the target surface, and $N_2$ adsorption gradually gives way to N-containing ion sub-plantation and N deposition. In particular, the proportion of ion sub-plantation increases from 25% to 37% during cathode erosion and dominates target poisoning. The coverage rate of compounds on the target surface rises all the time and aggravates target poisoning.

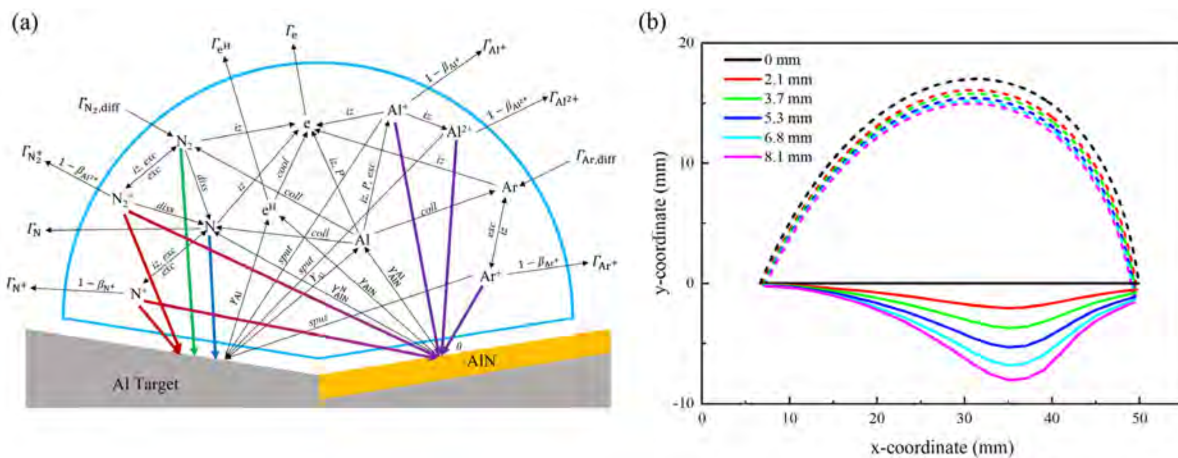


**FIG. 2.** (a) Schematic diagram of the global model for reactive sputtering on an Al target in the Ar/$N_2$ atmosphere. The area surrounded by the light blue lines represents the plasma ionization region. The arrows represent the reaction mechanisms: green for $N_2$ molecule adsorption, blue for N atom deposition, red for $N_2^+$ and $N^+$ ion sub-plantation, and purple for ion sputtering, and the change from red to purple indicates the coexistence of ion sub-plantation and sputtering. (b) Plasma ionization regions constructed based on the cathode erosion profiles, where solid lines represent the actual erosion profile and dashed lines are the magnetic field lines.


© Author(s) 2025

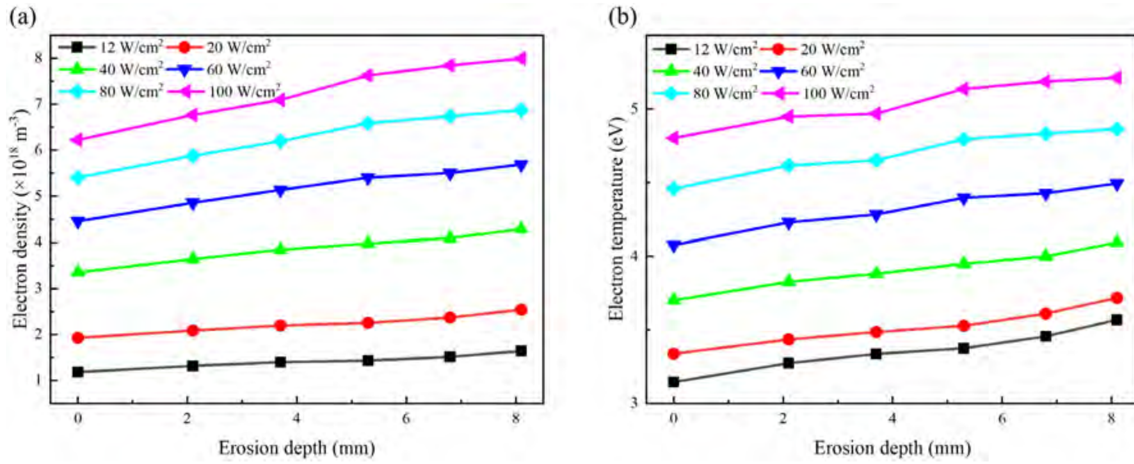


**FIG. 3.** (a) Electron densities and (b) electron temperature vs erosion depth for different power densities.

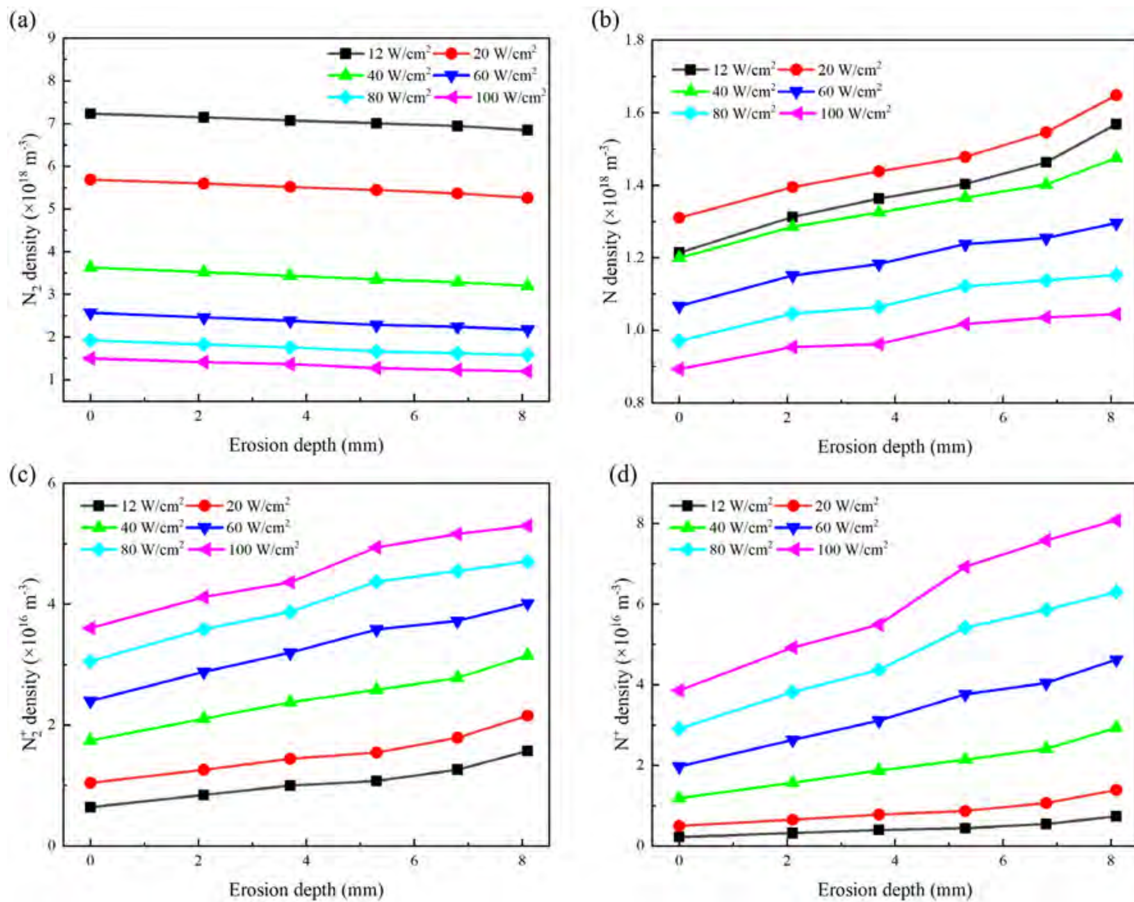


**FIG. 4.** Densities of reactive gas particles vs erosion depth for different power densities: (a) $N_2$ molecules, (b) N atoms, (c) $N_2^+$ ions, and (d) $N^+$ ions.


© Author(s) 2025

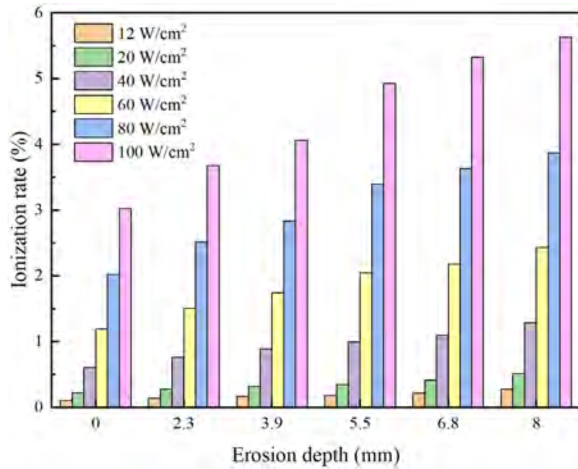


**FIG. 5.** Ionization rates of N vs erosion depth for different power densities.

## II. METHODS

### A. Voltage–current measurements

The plasma global model[14,15] accepts the current and voltage as the input.[16] According to Wendt *et al.*[17] and Lieberman *et al.*,[18] nearly no difference occurs in the erosion profile using different discharge powers when the erosion depth is the same. For this, we etched only one target at 100 W/cm$^2$ to record the erosion morphology at different depth. The volt-ampere characteristics at the power density of 12, 20, 40, 60, 80, and 100 W/cm$^2$ are tested to serve as the input for the global model. A 60 kW DC power supply (Ascent 60, Advanced Energy, USA) is used to perform high power density (100 W/cm$^2$) discharge on a rectangular cathode (300 × 123 mm$^2$).[19] The vacuum chamber dimensions are 600 × 600 × 500 mm$^3$, and the cathode target is Al (99.9% pure). Ar (99.99% pure, 45 SCCM) and $N_2$ (99.999% pure, 5 SCCM) are the working gas and reactive gas at a pressure of 0.5 Pa. Figures 1(a) and 1(b) show the erosion profiles and the volt-ampere characteristics, respectively.

### B. Global model with iterative modification of an erosion profile

The traditional global model assumes that the plasma ionization region is a semicircle with the erosion runway width as the diameter.[16] Therefore, the variations of the target surface morphology and the magnetic field caused by cathode erosion are not taken into consideration. All the etching morphologies are measured by vernier caliper, which are regarded as parts of the boundary of the IR region in global model because the sheath layer is very thin[18] and it is always neglected. The both ends of the cross section of the etched runway are always used to distinguish the main discharge area, so the magnetic field line passing through these two ends is assumed to be the other part of the IR region boundary. The closed region approximating a sector surrounded by the magnetic field line and cathode erosion profile is defined as the plasma ionization region, as shown in Fig. 2(a). Based on the different erosion profiles measured experimentally, geometric information of the plasma ionization region is obtained in different erosion stages, as shown in Fig. 2(b). The changed parameters are the average magnetic field intensity of the target surface $B$ (T), the ionization region volume $V_{IR}$ (m$^3$), the ionization region superficial area $S_{IR}$ (m$^2$), and the contact area of the ionization region with the target $S_T$ (m$^2$), and their evolutions are shown in Fig. 10 (in the Appendix). The IR region parameters obtained from the erosion depth of 0, 2.1, 3.7, 5.3, 6.8, and 8.1 mm are calculated to achieve the iterative process. In this way, the erosion process of reactive sputtering can be described by the model.

In the plasma system of reactive sputtering of an Al target in the Ar/$N_2$ atmosphere, the basic particles include cold electrons (e), hot electrons ($e^H$), ground-state neutral particles (Ar, $N_2$, N, and Al), excited-state neutral particles ($Ar^m$ and $N_2^m$), hot atoms ($Ar^H$), and ions ($Ar^+$, $N_2^+$, $N^+$, $Al^+$, and $Al^{2+}$). Based on the generation and consumption reactions, and the energy variations of each component,

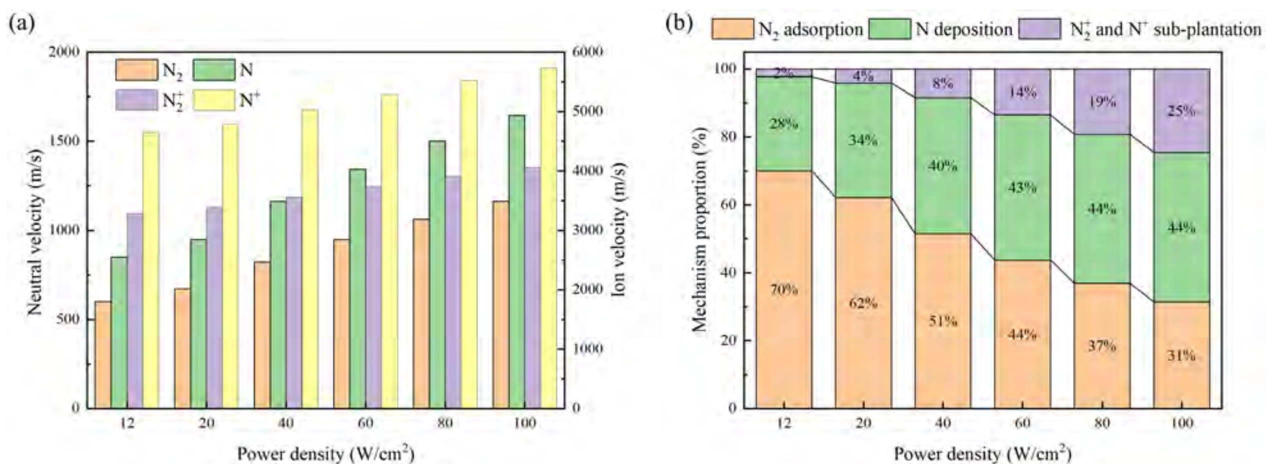


**FIG. 6.** Initial stage of reactive sputtering: (a) Velocities of $N_2$ molecules, N atoms, $N_2^+$ ions, and $N^+$ ions flowing toward the target surface; (b) proportions of $N_2$ molecule adsorption, N atom deposition, and $N_2^+$ and $N^+$ ion sub-plantation in target surface combination for different power densities.


© Author(s) 2025

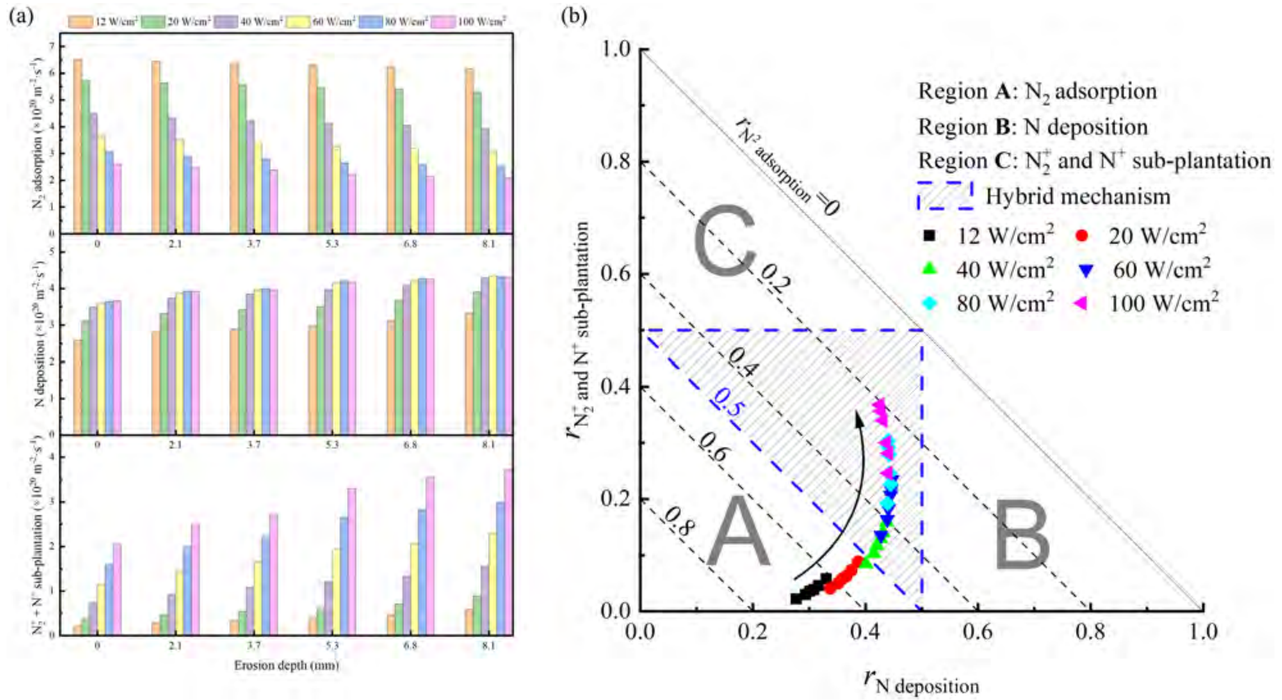


**FIG. 7.** (a) Fluxes and (b) proportions of $N_2$ molecule adsorption, N atom deposition, and $N_2^+$ and $N^+$ ion sub-plantation vs erosion depth for different power densities.

particle balance equations and energy balance equations are established to solve the density variation of the components in the complex system.

According to the interactions among various components in the system, the main formation and consumption processes of the compounds on the target surface can be obtained, namely, $N_2$ gas adsorption, N atom deposition, $N_2^+$ and $N^+$ ion sub-plantation, and ion sputtering, which are represented by the green, blue, red, and purple arrows in Fig. 2(a), respectively. To simplify the calculation, it is assumed that the compound formed on the target surface is the single AlN phase (see Fig. 11 in the Appendix). On this basis, the equilibrium equation for the target surface compound coverage rate $\theta$ can be obtained to characterize the target poisoning state, as shown as follows:[6,20,21]

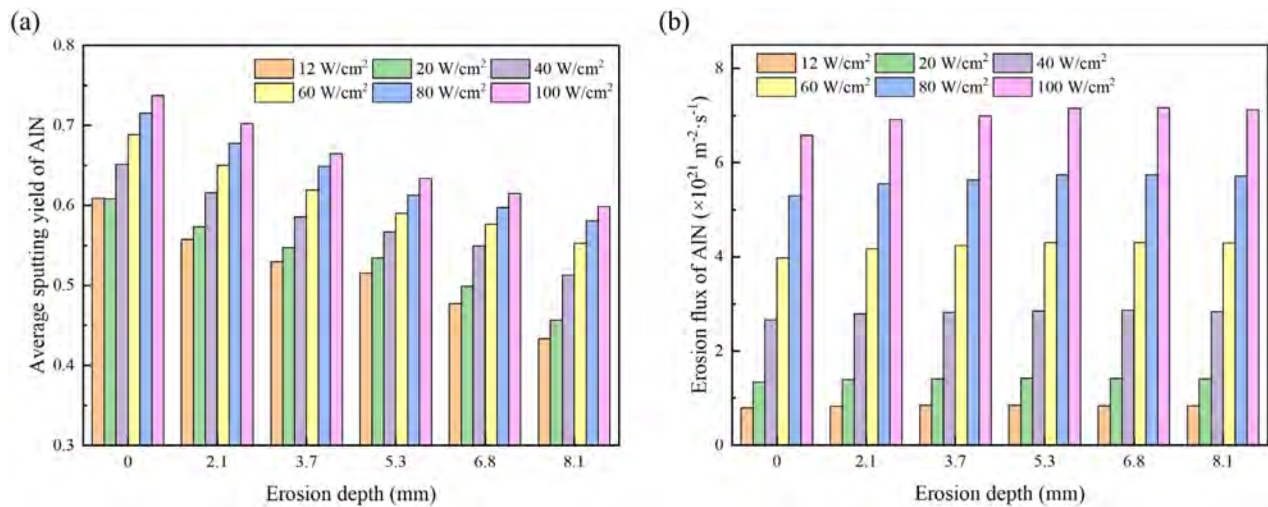


**FIG. 8.** (a) Average sputtering yields and (b) erosion fluxes of target surface compounds vs erosion depth for different power densities.


© Author(s) 2025

$$\frac{d\theta}{dt}\sigma_{Nt} = \boldsymbol{\Gamma}_{N_2,\text{absorption}}(1-\theta) + \boldsymbol{\Gamma}_{N,\text{deposition}}(1-\theta) + \boldsymbol{\Gamma}_{N_2^+ + N^+,\text{implantation}} - \boldsymbol{\Gamma}_{AlN,\text{sput}}\theta$$
$$= (2\alpha_{N_2})(\boldsymbol{\Gamma}_{N_2} + \boldsymbol{\Gamma}_{N_2^m}))(1-\theta) + \alpha_N \boldsymbol{\Gamma}_N(1-\theta) + (2\boldsymbol{\Gamma}_{N_2^+} + \boldsymbol{\Gamma}_{N^+}) - \boldsymbol{\Gamma}_{AlN,\text{sput}}\theta, \quad (1)$$

where $\Gamma$ ($m^{-2} s^{-1}$) represents the particle flux. $\sigma_{Nt} = 1.25 \times 10^{20}$ $m^{-2}$ is the saturation surface density of N atoms in the target surface compound AlN, and $\alpha$ is the sticking coefficient representing the probability of gas-neutral particles adsorbed by the target surface to form compounds. For $N_2$ molecules and N atoms, $\alpha$ can be set as 0.3 and 1,[6] respectively. This indicates that the adsorption efficiency of N atoms is 100%, which is equivalent to N atom deposition on the target surface. $\boldsymbol{\Gamma}_{AlN,sput}$ ($m^{-2} s^{-1}$) is the flux of the target surface compound AlN consumed by ion sputtering, as shown as

$$\boldsymbol{\Gamma}_{AlN,\text{sput}} = N^N_{A1N} \sum \boldsymbol{\Gamma}_{\text{ion}} Y^N_{\text{ion,AlN}},$$
$$\text{ion} = Ar^+,\ A1^+, A1^{2+}, N^+ \text{ or } N_2^+, \quad (2)$$

where $N^N_{AlN} = 1$ is the number of N atoms in an AlN molecule and $Y^N_{ion,AlN}$ represents the sputtering yield of N atoms on the compound (see Fig. 12 in the Appendix). More specific details of the model are given in the Appendix.

## III. RESULTS AND DISCUSSION

The plasma evolution behavior during the erosion process is simulated by the global model with iterative modification of the erosion profile. The electron density and electron temperature are shown in Figs. 3(a) and 3(b), respectively. It is evident that with increasing power density from 12 to 100 W/cm$^2$, the electron density in the plasma system rises from $1.2\text{–}1.6 \times 10^{18}$ to $6.2\text{–}8.0 \times 10^{18}$ $m^{-3}$, representing an increase of about four times. Meanwhile, the electron temperature rises from 3.1–3.6 to 4.8–5.2 eV of about 1/2. The phenomenon is consistent with the plasma properties for high power discharges.[6,13,19] The increase in electron density and electron temperature enhances the ionization rate of neutral particles in the plasma. At a constant power density, both the electron density and electron temperature increase at the deeper erosion stage, indicating further enhancement in the discharge intensity. This is because the target surface becomes thinner with erosion, and the magnetic field of the target surface is larger thus enhancing electron binding. However, since the discharge voltage decreases at deeper erosion stage, the acceleration effect on electrons weakens, resulting in a slight increase in the electron density and electron temperature.

Figure 4 shows the densities of various reactive gas particles in the plasma at different erosion depths for different power densities. With increasing power density, the higher electron density and electron temperature promote the ionization and dissociation reactions of $N_2$ molecules.[13,22] Meanwhile, the background temperature near the target surface increases, and the sputtering intensity goes up, resulting in a strong gas rarefaction effect[23] which causes a substantial decrease in the $N_2$ density. However, at a constant power density, the gas rarefaction effect is basically unaffected by the cathode erosion. Therefore, the increase in electron density and electron temperature plays a dominant role at this point, which promotes $N_2$ molecule density to gradually decrease at deeper erosion stage. N atoms, $N_2^+$ ions, and $N^+$ ions are generated by ionization and dissociation of $N_2$ molecules during electron impact, and their densities rise with power density and erosion depth. Differently, the N atom density decreases when the power density exceeds 20 W/cm$^2$. This is because the gas rarefaction effect and the enhanced sticking of N, resulting in an increased consumption which is more than the generation by $N_2$ dissociation. At low power density, both electron density and electron temperature are low, resulting in weak electron impact reactions. Since $N^+$ ions are generated by the dissociation of $N_2$ molecules and ionization of N atoms in turn, the density of $N^+$ ions is lower than that of $N_2^+$ ions at low power density and increases slightly with the small increase in electron density and electron temperature at the deeper erosion stage. However, with increasing electron density and electron temperature, the generation of $N^+$ ions is enhanced, while $N_2^+$ ions are further consumed by dissociation reactions. Therefore, at high power densities, the density of $N^+$ exceeds that of $N_2^+$, presenting a greater increase at deeper erosion stage.

The ionization rates of N for different erosion depths at different power densities are calculated by Eq. (3), as shown in Fig. 5,

$$\alpha_{N\ \text{element}} = \frac{n_{N_2^+} + n_{N^+}}{n_{N_2} + n_N + n_{N_2^+} + n_{N^+}} \times 100\%. \quad (3)$$

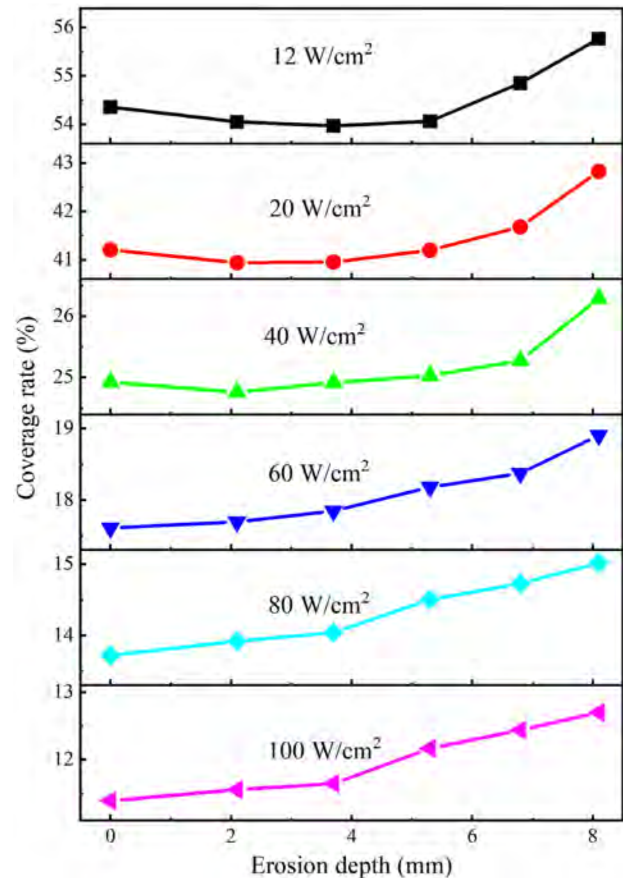


**FIG. 9.** Coverage rates of target surface compounds vs erosion depth for different power densities.


© Author(s) 2025

**TABLE I.** Rate coefficients for Ar/$N_2$/Al plasma.

| Reaction equation | Rate coefficient $k$ ($m^3 \cdot s^{-1}$) | Threshold (eV) | Reference |
|---|---|---|---|
| $e + Ar \rightarrow Ar^+ + 2e$ | $k_{iz} = 2.3\times10^{-14}T_e^{0.59}\exp(-17.44/T_e)$ | $E_{iz} = 15.76$ | 27 |
| $e^H + Ar \rightarrow Ar^+ + 2e$ | $k_{iz}^H = 8\times10^{-14}T_e^{0.16}\exp(-27.53/T_e)$ | $E_{iz} = 15.76$ | 27 |
| $e + Ar \rightarrow Ar^m + e$ | $k_{ex} = 2.5\times10^{-15}T_e^{0.74}\exp(-11.56/T_e)$ | $E_{ex} = 11.56$ | 28 |
| $e^H + Ar \rightarrow Ar^m + e$ | $k_{ex}^H = 3.84\times10^{-14}T_e^{-0.68}\exp(-22.32/T_e)$ | $E_{ex} = 11.56$ | 28 |
| $e + Ar \rightarrow Ar + e$ | $k_{el} = 2.336\times10^{-14}T_e^{1.609}\times\exp(0.0618(\ln T_e)^2 - 0.1171(\ln T_e)^3)$ | | 28 |
| $e + Ar^m \rightarrow Ar + e$ | $k_{dex} = 4.3\times10^{-16}T_e^{0.74}$ | $E_{dex} = -11.56$ | 29 |
| $e + Ar^m \rightarrow Ar^+ + 2e$ | $k_{miz} = 6.8\times10^{-15}T_e^{0.67}\exp(-4.2/T_e)$ | $E_{miz} = 4.2$ | 28 |
| $e^H + Ar^m \rightarrow Ar^+ + 2e$ | $k_{miz}^H = 5.7\times10^{-13}T_e^{-0.33}\exp(-6.82/T_e)$ | $E_{miz} = 4.2$ | 28 |
| $e + N_2 \rightarrow N_2^+ + 2e$ | $k_{iz,N_2} = k_{iz,N_2}^H = 1.95\times10^{-15}T_e^{1.13}\exp(-14.4/T_e)$ | $E_{iz,N_2} = 15.6$ | 30 |
| $e + N_2 \rightarrow N_2^m + e$ | $k_{ex,N_2} = k_{ex,N_2}^H = 5.81\times10^{-15}\exp(-7.57/T_e)$ | $E_{ex,N_2} = 6.17$ | 30 |
| $e + N_2 \rightarrow N_2 + e$ | $k_{el,N_2} = 1.04\times10^{-13}T_e^{0.43}\exp(-0.206/T_e)$ | | 31 |
| $e + N_2 \rightarrow 2N + e$ | $k_{diss} = 6.15\times10^{-15}T_e^{0.81}\exp(-12.8/T_e)$ | $E_{diss} = 9.76$ | 32 |
| $e + N_2^+ \rightarrow 2N$ | $k_{diss2} = 1.9\times10^{-15}T_e^{0.30}$ | | 33 |
| $e + N_2^m \rightarrow N_2^+ + 2e$ | $k_{iz,N_2^m} = k_{iz,N_2^m}^H = 3.39\times10^{-13}T_e^{-0.176}\exp(-32.4/T_e)$ | $E_{iz,N_2^m} = 9.43$ | 30 |
| $e + N \rightarrow N^+ + 2e$ | $k_{iz,N} = 3.84\times10^{-15}T_e^{0.92}\exp(-12.1/T_e)$ | $E_{iz,N} = 14.54$ | 30 |
| $e + N \rightarrow N + e$ | $k_{el,N} = 2.18\times10^{-13}T_e^{-0.84}\exp(-0.685/T_e)$ | | 30 |
| $N_2 + N^+ \rightarrow N + N_2^+$ | $k_{N_2-N^+} = 2.0\times10^{-17}$ | | 30 |
| $N_2^+ + N \rightarrow N^+ + N_2$ | $k_{N_2^+-N} = 1.0\times10^{-17}$ | | 30 |
| $N_2^m + N \rightarrow N + N_2$ | $k_{N_2^m-N} = 4.0\times10^{-17}$ | $E_{dex,N_2^m} = -6.17$ | 30 |
| $N_2^m + N_2 \rightarrow 2N_2$ | $k_{N_2^+-N_2} = 3.5\times10^{-18}$ | $E_{dex,N_2^m} = -6.17$ | 30 |
| $N_2^m \rightarrow N_2 + h\nu$ | $k_{dex,N_2^m} = 2.3\times10^{-4}$ | $E_{dex,N_2^m} = -6.17$ | 30 |
| $Ar^+ + N_2 \rightarrow Ar + N_2^+$ | $k_{Ar^+-N_2} = 1.2\times10^{-17}$ | | 30 |
| $e + Al \rightarrow Al^+ + 2e$ | $k_{iz,Al} = \exp(-E_{iz,Al}/T_e)\times(T_e/E_{iz,Al})\sum_{n=0}^{5}a_n[\log_{10}(T_e/E_{iz,Al})]^n$ | $E_{iz,Al} = 5.96$ | 34 |
| $e + Al^+ \rightarrow Al^{2+} + 2e$ | $k_{iz,Al^+} = \exp(-E_{iz,Al^+}/T_e)\times(T_e/E_{iz,Al^+})\sum_{n=0}^{5}a_n[\log_{10}(T_e/E_{iz,Al^+})]^n$ | $E_{iz,Al^+} = 18.83$ | 34 |
| $Ar^m + Al \rightarrow Al^+ + Ar + e$ | $k_P = 5.9\times10^{-16}$ | $E_P = -5.60$ | 35 |
| $Ar^+ + Al \rightarrow Al^+ + Ar$ | $k_{chexc} = 1.0\times10^{-15}$ | | 35 |

The ionization rate of N is positively correlated with both the power density and erosion depth. At a low power density (12 W/cm$^2$), the ionization rate of N increases slightly from 0.10% to 0.27% due to the small increase in $N^+$ and $N_2^+$ ion density at the deeper erosion stage. The low ionization rate further indicates that the ionization of reactive gas shows almost no effect on the plasma system at this time. The result is consistent with the basic assumption in the Berg model that ionization of the reactive gas can be ignored.[7] In contrast, at a high power density (100 W/cm$^2$), the ionization rate of N increases from 3.0% to 5.6% during reactive sputtering, which is approximately 15–30 times larger, indicating that the effect of reaction gas ionization cannot be ignored.

To study the formation process of the target surface compounds, the velocities of $N_2$ molecules, N atoms, $N_2^+$ ions, and $N^+$ ions flowing from the ionization region toward the target surface initially (erosion depth of 0 mm) are calculated, as shown in Fig. 6(a). The ion velocity is the Bohm velocity determined by the electron temperature $T_e$ (eV),[18] while the neutral particle velocity is the thermal velocity determined by the background temperature $T_{IR}$ (K) in the ionization region (see the Appendix), as shown as

$$u_{Bohm} = \sqrt{eT_e/m_{ion}}, \quad (4)$$

$$u_{Thermal} = \sqrt{8k_b T_{IR}/m_{neu}},\ neu = N_2 \text{ or } N, \quad (5)$$

where $k_b = 1.38\times10^{-23}$ J/K is Boltzmann's constant and $m$ (kg) is the particle mass. Since $eT_e \gg k_b T_{IR}$, the ion velocity is larger than that of neutral particles. With increasing power density, the electron temperature and background temperature increase, resulting in a gradual increase in the velocities of all the components. According to the densities and velocities of the reactive gas components, the fluxes of $N_2$ molecule adsorption, N atom deposition, and $N_2^+$ and $N^+$ ion sub-plantation are obtained by the empirical formulas in Eqs. (6)–(8), respectively,[6]

$$\Gamma_{N_2,adsorption} = 2\alpha_{N_2}(\Gamma_{N_2} + \Gamma_{N_2^m}) = 2\alpha_{N_2}\frac{(n_{N_2} + n_{N_2^m})}{4}u_{N_2,thermal}, \quad (6)$$

$$\Gamma_{N,deposition} = \alpha_N \Gamma_N = \alpha_N n_N u_{N,thermal}, \quad (7)$$

$$\Gamma_{N_2^++N^+,implantation} = 2\Gamma_{N_2^+} + \Gamma_{N^+} = 0.4(2n_{N_2^+}u_{N_2^+,Bohm} + n_{N^+}u_{N^+,Bohm}). \quad (8)$$


© Author(s) 2025

Consequently, in the initial stage of reactive sputtering, the proportions of the three main reactions in the formation of the target surface compounds at different power densities can be obtained, as shown in Fig. 6(b). At a small power density (12 W/cm$^2$), $N_2$ molecule adsorption and N atom deposition account for 70% and 28%, respectively, thus dominating the target surface combination. At this point, the ion density is three orders of magnitude less than that of neutral particles, with the proportion of $N_2^+$ and $N^+$ ion sub-plantation of only 2%. With increasing power density, the ion density rises, while the neutral particle density decreases. When the power density reaches 100 W/cm$^2$, the ion density is only one order of magnitude less than that of neutral particles. Coupling with the particle velocities, the proportions of $N_2$ molecule adsorption, N atom deposition, and $N_2^+$ and $N^+$ ion sub-plantation are 31%, 44%, and 25%, respectively. Hence, in high-power reactive sputtering, the dominant factors of target surface combination shift from $N_2$ molecule adsorption to a combination of N atom deposition and N-containing ion sub-plantation.

Figure 7(a) shows the fluxes of $N_2$ molecule adsorption, N atom deposition, and $N_2^+$ and $N^+$ ion sub-plantation vs erosion depth for different power densities. As cathode erosion proceeds, the flux of $N_2$ molecule adsorption decreases, while the fluxes of N atom deposition and $N_2^+$ and $N^+$ ion sub-plantation increase. At a small power density (12 W/cm$^2$), the variations of the three processes are relatively small, thereby maintaining stability throughout the reactive sputtering process. In contrast, at a large power density (100 W/cm$^2$), the flux of $N_2^+$ and $N^+$ ion sub-plantation increases from $2.1 \times 10^{20}$ to $3.7 \times 10^{20}$ $m^{-2}\,s^{-1}$ by 76%. In comparison, the variation in $N_2$ molecule adsorption and N atom deposition is less than $5 \times 10^{19}$ $m^{-2}\,s^{-1}$, indicating that the high-power discharge mainly enhances the contribution of $N_2^+$ and $N^+$ ion sub-plantation to the target surface combination. The proportions of the three reactions in surface combination are statistically summarized in Fig. 7(b), in which regions **A**, **B**, and **C** indicate that the target surface combination is dominated by $N_2$ molecule adsorption, N atom deposition, and $N_2^+$ and $N^+$ ion sub-plantation, respectively. The shaded area between regions **A**, **B**, and **C** indicates that the three mechanisms dominate the target surface combination together. The direction of the black arrow represents the deepening of cathode erosion, revealing a gradual decrease in the proportion of $N_2$ molecule adsorption along the arrow direction. Discharges at lower power densities (12 and 20 W/cm$^2$) are located in region **A**, and the fitted lines show a small slope, indicating that N atom deposition mainly increases at deeper erosion stage. With increasing power density, the discharge gradually enters the shaded area, with a significant increase in the slope of the fitted lines indicating that the increase is mainly in

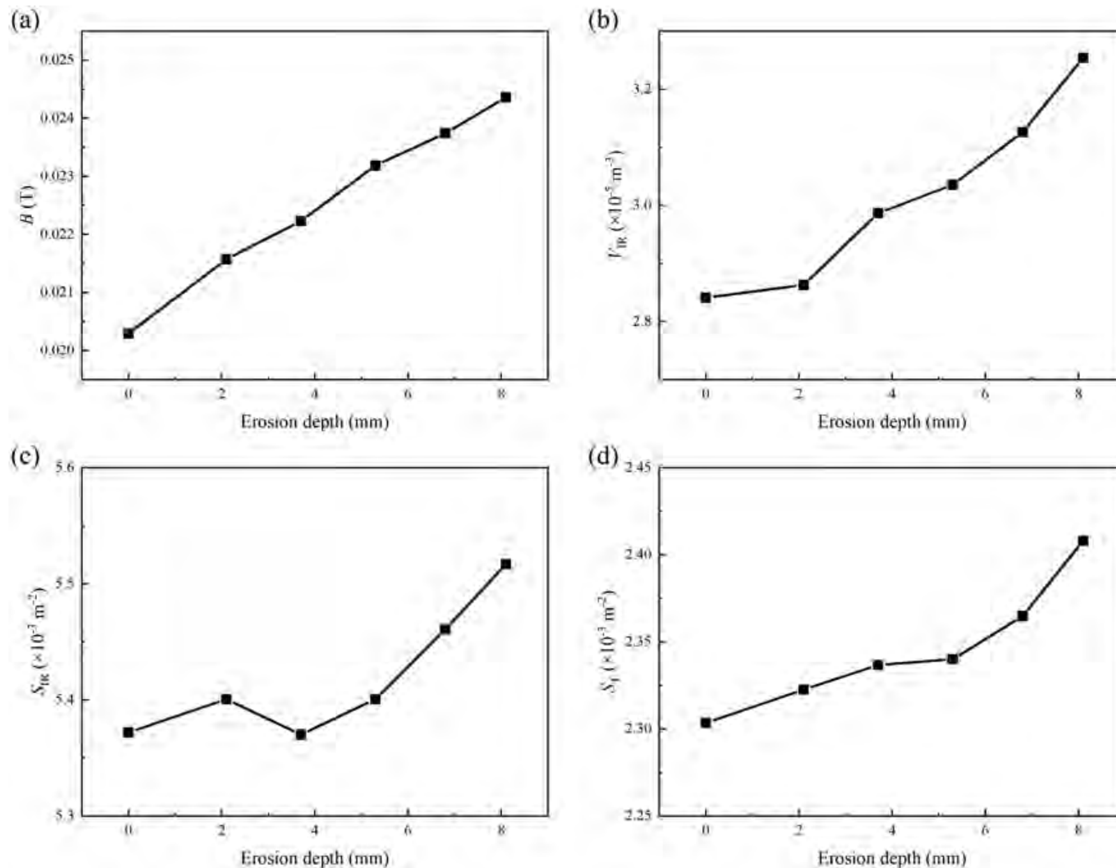


**FIG. 10.** (a) The average magnetic field intensity of the target surface *B* (T) (b) the ionization region volume $V_{IR}$ (m$^3$) (c) the ionization region superficial area $S_{IR}$ (m$^2$), and (d) the contact area of the ionization region with the target $S_T$ (m$^2$) at different erosion depth.


© Author(s) 2025

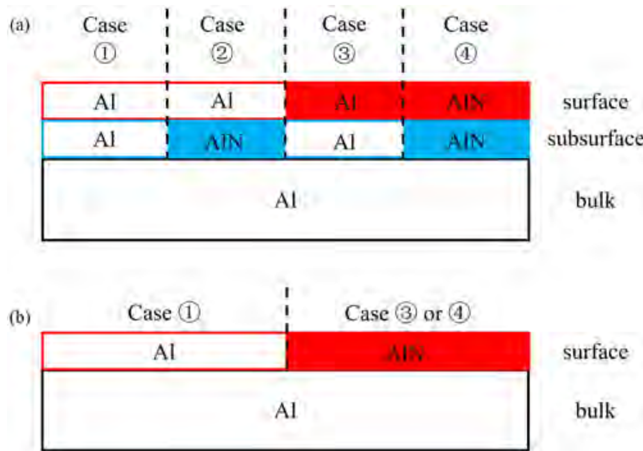


FIG. 11. (a) Conventional and (b) simplified schematic diagram of the target component in reactive sputtering.

$N_2^+$ and $N^+$ ion sub-plantation. $N^+$ and $N_2^+$ ions penetrate into the subsurface under the effect of sheath voltage, and provide 1 and 2 N atoms to form the compound, respectively. Yet/However the sputtering of the compound is very small because of the small sputtering yields of $N^+$ and $N_2^+$ ion of less than 1. Therefore, the target poisoning could be promoted by $N^+$ and $N_2^+$ ion sub-plantation. When the power density is 100 W/cm$^2$, the fitted line is almost perpendicular to the horizontal axis of the coordinate system, indicating that N atom deposition no longer increases. Consequently, the proportion of $N_2^+$ and $N^+$ ion sub-plantation significantly increases from 25% to 37%, and it is the main reason for the variations in the target poisoning states. According to the tendency revealed in Fig. 7(b), if the power density is further increased to above 100 W/cm$^2$, the discharge will enter region **C**, in which the target surface combination is dominated by $N_2^+$ and $N^+$ ion sub-plantation, and so is target poisoning.

Figure 8 shows the average sputtering yield and total sputtering flux of various ions in the sputtering of the target surface compounds vs erosion depth for different power densities. With increasing power density, the rise in target voltage leads to higher sputtering energy to the sputtering ions, leading to an increase in the average sputtering yield. However, at a constant power density, the target voltage gradually decreases at deeper erosion stage, which reduces the average sputtering yield of the target surface compounds. In addition, more N-containing ions participate in sputtering and contribute to the decrease in the average sputtering rate. According to Eq. (2), the sputtering flux of ions on the target surface compounds depends on the number of sputtering ions and their average sputtering yield. With increasing power density, both the number of ions involved in sputtering and the average sputtering rate increase, and the sputtering flux of the target surface compounds is enhanced. At a constant power density, the discharge intensity and ionization rate increase at deeper erosion stage to raise the number of sputtering ions. However, the target voltage decreases simultaneously, resulting in a reduced average sputtering yield. As a result, the effects counteract each other and the sputtered flux is basically constant, showing only a slight variation. Generally, the sputtered flux of the target surface compounds increases at small erosion depths, but gradually stabilizes with deepened erosion or even decreases slightly at large erosion depths due to the faster erosion.

Given that the timescale for the plasma to reach a steady state is extremely small ($1 \times 10^{-3}$ s), the erosion profile variation during the measurement period is negligible. Therefore, when the plasma discharge reaches a steady state, it can be assumed that the components in the plasma system no longer change with time. At this time, the generation and consumption of the target surface compounds reach a

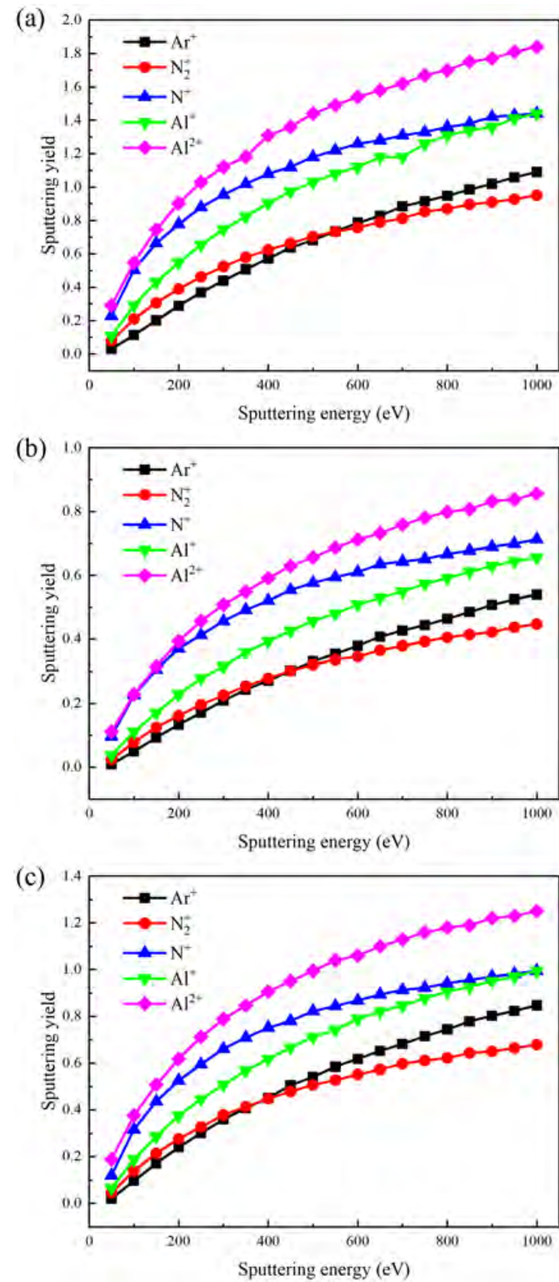


FIG. 12. The sputtering yield of (a) Al atoms on Al target, (b) Al atoms, and (c) N atoms on the AlN compound.


© Author(s) 2025

balance.[13] According to Eq. (1), the coverage rate $\theta$ of the target surface compound can be obtained as

$$\theta = \frac{\Gamma_{N_2,\,adsorption} + \Gamma_{N,\,deposition} + \Gamma_{N_2^+ + N^+,\,implantation}}{\Gamma_{N_2,\,adsorption} + \Gamma_{N,\,deposition} + \Gamma_{AlN,\,sput}} = \frac{1 + \dfrac{\Gamma_{N_2^+ + N^+,\,implantation}}{\Gamma_{N_2,\,adsorption} + \Gamma_{N,\,deposition}}}{1 + \dfrac{\Gamma_{AlN,\,sput}}{\Gamma_{N_2,\,adsorption} + \Gamma_{N,\,deposition}}}. \quad (9)$$

Figure 9 shows the coverage rate of the target surface compound vs erosion depth for different power densities. At a low power density of 12 W/cm$^2$, $N_2^+$ and $N^+$ ion sub-plantation is minimal, and the behavior of N-containing particles involved in the target surface combination remains essentially unchanged, meaning that the generation of the target surface compound basically remains constant.[4] At this time, ion sputtering determines the coverage rate of the target surface compound. According to Eq. (9), the coverage rate $\theta$ is inversely related to the AlN sputtering flux, showing a trend of first decreasing and then increasing with deepened erosion. However, at a large power density (100 W/cm$^2$), the $N_2^+$ and $N^+$ ion sub-plantation flux significantly increases at deeper erosion stage, and the ion reactivity with the target is far beyond that of $N_2$ molecules and N atoms. In addition, the effect of the enhancement in $N_2^+$ and $N^+$ ion sub-plantation on the target surface combination is larger than the effect of decreased sputtering yields on the erosion speed. Consequently, the coverage rate $\theta$ rises all the time, resulting in more severe target poisoning. This result explains the phenomenon in high-power reactive sputtering, in which as soon as target poisoning causes discharge extinguishing, it is difficult to resume with the automatic restart function of the sputtering power source using the same startup power. Therefore, high-power magnetron sputtering power sources have to provide higher energy for reignition in order to enable automatic restarting of the discharge, that is, larger excitation pulses. In addition, it can be further inferred from this result that the discharge stability and the coating consistency may change at deeper erosion stage, which is detrimental to industrial production. In order to maintain the stability, this work can provide a strategy to control the power density according to the extent of cathode etching.

## IV. CONCLUSION

To address the unstable and discontinuous discharge caused by plasma evolution during the reactive sputtering, we take the reactive sputtering of the Al target in the Ar/$N_2$ atmosphere as an example and establish a global model with iterative modification of the erosion profile to improve the simulation accuracy, by which the plasma evolution and target surface combination behavior during erosion using different power densities are investigated. With increasing power density, the electron density and electron temperature in the plasma increase to enable more reactive gas ions to participate in the target surface combination. The proportion of $N_2$ molecule adsorption involved in target surface combination decreases, whereas the proportion of N atom deposition and N-containing ion sub-plantation increases. During erosion, the proportion of N involved in target surface combination remains essentially unchanged at low power densities, but the proportion of N-containing ion sub-plantation increases from 25% to 37% at high power densities, thus dominating target poisoning. The calculated generation and consumption of target surface compounds indicate that the coverage rate of target surface compounds decreases and then increases at low power densities, while that rises all the time at high power densities, leading to increasingly severe target poisoning. This explains the phenomenon that when target poisoning extinguishes the discharge in high-power reactive sputtering, it cannot be restarted automatically using the restart function of the sputtering power source (at the same startup power). The results provide insight into the design of high-power reactive sputtering power sources.

## ACKNOWLEDGMENTS

This work was financially supported by the Shenzhen Science and Technology Research Grants (Grant Nos. SGDX20201103095406024 and KJZD20231023100304009), the National Key R&D Program of China (Grant No. 2023YFA1608802), Sustainable Supporting Funds for Colleges and Universities in 2022 (Grant No. 20220810143642004), the National Natural Science Foundation Youth Science Fund Project (Grant No. 52305174), the Postdoctoral Research Fund Project after Outbound of Shenzhen (Grant No. 6700200201), the Shenzhen-Hong Kong Technology Cooperation Funding Scheme (TCFS) (Grant No. GHP/149/20SZ or CityU 9440296), City University of Hong Kong Internal Fund for ITF Projects (Grant No. 9678148), City University of Hong Kong Donation Research Grants (Grant Nos. DON-RMG 9229021 and 9220061), and City University of Hong Kong Strategic Research Grant (SRG) (Grant No. 7005505).

26 February 2025 14:26:00

## AUTHOR DECLARATIONS

### Conflict of Interest

The authors have no conflicts to disclose.

### Author Contributions

Suihan Cui, Dongjie Yang, and Shiyi Tang contributed equally to this work.

**Suihan Cui:** Conceptualization (equal); Software (equal); Writing – original draft (equal); Writing – review & editing (equal). **Dongjie Yang:** Investigation (equal). **Shiyi Tang:** Software (equal); Writing – original draft (equal); Writing – review & editing (equal). **Ziqi Ma:** Software (supporting). **Mengran Xiao:** Software (supporting). **Xiaokai An:** Investigation (supporting). **Wei Lv:** Funding acquisition (equal). **Wanli Luo:** Funding acquisition (equal). **Qinfang Yu:** Funding acquisition (equal). **Liangliang Liu:** Investigation (equal); Writing – original draft (equal). **Ricky K. Y. Fu:** Writing – review & editing (equal). **Paul K. Chu:** Writing – review & editing (equal). **Zhongzhen Wu:** Conceptualization (equal); Methodology (equal); Writing – original draft (equal); Writing – review & editing (equal).

## DATA AVAILABILITY

The data that support the findings of this study are available from the corresponding author upon reasonable request.

## APPENDIX: DETAILS OF THE GLOBAL MODEL

The reactions in the Ar/$N_2$/Al plasma system and their reaction rate coefficients are shown in Table I.


© Author(s) 2025

#### 1. Particle balance equations of atoms and ions

(1) Ar atom:

$$\frac{dn_{Ar}}{dt} = -(k_{iz}n_e + k_{iz}^H n_{e^H})n_{Ar} - (k_{ex}n_e + k_{ex}^H n_{e^H})n_{Ar} - \boldsymbol{\Gamma}_{Al,coll}\frac{m_{Al}}{m_{Ar}}\frac{n_{Ar}}{n_{gas}}\frac{S_{IR}-S_T}{V_{IR}} + k_{Ar^+-N_2}n_{Ar^+}n_{N_2} + k_{chexc}n_{Ar^+}n_{Al} + k_p n_{Ar^m}n_{Al} + (k_{dex}n_e + k_{dex}^H n_{e^H})n_{Ar^m} + \boldsymbol{\Gamma}_{Ar,diff}\frac{S_{IR}-S_T}{V_{IR}}, \quad (A1)$$

where $n$ ($m^{-3}$) is the number density of particles in the plasma system. $V_{IR}$ ($m^3$) is the ionization region volume, $S_{IR}$ ($m^2$) is the ionization region superficial area, and $S_T$ ($m^2$) is the contact area of the ionization region with the target. $n_{gas} = n_{Ar} + n_{Ar^m} + n_{Ar^H} + n_{N_2} + n_{N_2^m} + n_N$ is the density of neutral gas particles. $\boldsymbol{\Gamma}_{Ar,diff}$ ($m^{-2}\,s^{-1}$) describes the diffusional Ar flux, as shown as[19]

$$\boldsymbol{\Gamma}_{Ar,\,diff} = \frac{n_{Ar,\,0}u_{Ar,\,0} - n_{Ar}u_{Ar}}{4}, \quad (A2)$$

where $u_{Ar,\,0} = \sqrt{\frac{8k_b T_0}{\pi m_{Ar}}}$ and $u_{Ar} = \sqrt{\frac{8k_b T_{IR}}{\pi m_{Ar}}}$ is the average velocity of Ar out and in the ionization region, respectively. The temperature distribution by the plasma heat transfer model according to Ref. 36, $T_0$ (K) and $T_{IR}$ (K) is evaluated by the average background temperature out and in the ionization region, respectively, both increasing with the power density and calculated with finite element method. $\boldsymbol{\Gamma}_{Al,coll}$ ($m^{-2}\,s^{-1}$) stands for the collision part of the Al, $Al^+$, and $Al^{2+}$ sputtering wind, as shown as

$$\boldsymbol{\Gamma}_{Al,coll} = (\boldsymbol{\Gamma}_{Al,sput} + \boldsymbol{\Gamma}_{Al^+,sput} + \boldsymbol{\Gamma}_{Al^{2+},sput})F_{coll},$$
$$\boldsymbol{\Gamma}_{M,sput} = \frac{n_M u_{T_{Al}}}{4}, M = Al, Al^+, \text{and } Al^{2+},$$
$$u_{T_{Al}} = (3k_B T/m_{Al})^{1/2}, \quad (A3)$$
$$F_{coll} = 1 - \exp(-R_{IR}(\sigma_{Ar-Al}(n_{Ar} + n_{Ar^m} + n_{Ar^H}) + \sigma_{Ar-N_2}(n_{N_2} + n_{N_2^m}) + \sigma_{Ar-N}n_N)),$$

where $F_{coll}$ (Hz) is the collision probability of Al particles with neutral gas particles in the ionization region, $u_{T_{Al}}$ (m/s) is the root mean square velocity, $\sigma$ ($m^2$) is the cross section of collision based on the hard sphere model, and $R_{IR}$ (m) is the thickness of the ionization region.

(2) $Ar^+$ ion:

$$\frac{dn_{Ar^+}}{dt} = -k_{Ar^+-N_2}n_{Ar^+}n_{N_2} - k_{chexc}n_{Ar^+}n_{Al} - \boldsymbol{\Gamma}_{Ar^+}\frac{S_T}{V_{IR}} - \boldsymbol{\Gamma}_{Ar^+}\frac{(S_{IR}-S_T)(1-\beta_{Ar^+})}{V_{IR}} + (k_{iz}n_e + k_{iz}^H n_{e^H})(n_{Ar} + n_{Ar^H}) + (k_{miz}n_e + k_{miz}^H n_{e^H})n_{Ar^m}, \quad (A4)$$

where $\boldsymbol{\Gamma}_{Ar^+} = 0.4n_{Ar^+}u_{Ar^+,\,Bohm}$ is the $Ar^+$ flux leaving the ionization region and $\beta_{Ar^+}$ is the ion return probability can be expressed as

$$\beta_{ion} = \begin{cases} 0, & U_{IR} \le T_{ion}/q_{ion}, \\ 1 - \dfrac{T_{ion}}{U_{IR}q_{ion}}, & U_{IR} > T_{ion}/q_{ion}, \end{cases} \quad (A5)$$

in which $q_{ion}$ (eV) is the charge number of ion and $T_{ion}$ (eV) is the ion energy. $U_{IR}$ (V) is the voltage drop in the ionization region which could be calculated by the Poisson equation as

$$U_{IR} = -\frac{eR_{IR}^2}{\varepsilon_0}\left(n_{Ar^+} + n_{N_2^+} + n_{N^+} + n_{Al^+} + 2n_{Al^{2+}} - n_e - n_{e^H}\right), \quad (A6)$$

where $\varepsilon_0$=$8.85 \times 10^{-12}$ F/m is the vacuum dielectric constant.

(3) $Ar^m$ atom:

$$\frac{dn_{Ar^m}}{dt} = -(k_{miz}n_e + k_{miz}^H n_{e^H})n_{Ar^m} - k_P n_{Ar^m}n_{Al} - (k_{dex}n_e + k_{dex}^H n_{e^H})n_{Ar^m} - \boldsymbol{\Gamma}_{Al,coll}\frac{m_{Al}}{m_{Ar}}\frac{n_{Ar^m}}{n_{gas}}\frac{S_{IR}-S_T}{V_{IR}} - \boldsymbol{\Gamma}_{Ar^m,diff}\frac{S_{IR}-S_T}{V_{IR}} + (k_{ex}n_e + k_{ex}^H n_{e^H})(n_{Ar} + n_{Ar^H}), \quad (A7)$$

where $\boldsymbol{\Gamma}_{Ar^m,diff} = \frac{n_{Ar^m}}{4}u_{Ar}$ stands for the diffusional flux of $Ar^m$ atom.

(4) $Ar^H$ atom:

$$\frac{dn_{Ar^H}}{dt} = -(k_{iz}n_e + k_{iz}^H n_{e^H})n_{Ar^H} - (k_{ex}n_e + k_{ex}^H n_{e^H})n_{Ar^H} - \boldsymbol{\Gamma}_{Ar^H,diff}\frac{S_{IR}-S_T}{V_{IR}} - \boldsymbol{\Gamma}_{Al,coll}\frac{m_{Al}}{m_{Ar}}\frac{n_{Ar^H}}{n_{gas}}\frac{S_{IR}-S_T}{V_{IR}} + \boldsymbol{\Gamma}_{Ar^+}\frac{S_T}{V_{IR}}. \quad (A8)$$

(5) $N_2$ molecule:

$$\frac{dn_{N_2}}{dt} = -\left(k_{iz,\,N_2}n_e + k_{iz,\,N_2}^H n_{e^H}\right)n_{N_2} - \left(k_{ex,\,N_2}n_e + k_{ex,\,N_2}^H n_{e^H}\right)n_{N_2} - k_{diss}n_{N_2}n_e - k_{N_2-N^+}n_{N_2}n_{N^+} - k_{Ar^+-N_2}n_{Ar^+}n_{N_2} - \boldsymbol{\Gamma}_{Al,coll}\frac{m_{Al}}{m_{N_2}}\frac{n_{N_2}}{n_{gas}}\frac{S_{IR}-S_T}{V_{IR}} + k_{N_2^+-N}n_{N_2^+}n_N + k_{N_2^m-N}n_{N_2^m}n_N + k_{N_2^m-N_2}n_{N_2^m}n_{N_2} + k_{N_2^m-dex}n_{N_2^m} + \boldsymbol{\Gamma}_{N_2,diff}\frac{S_{IR}-S_T}{V_{IR}}. \quad (A9)$$

(6) $N_2^+$ ion:

$$\frac{dn_{N_2^+}}{dt} = -k_{diss2}n_{N_2^+}n_e - k_{N_2^+-N}n_{N_2^+}n_N - \boldsymbol{\Gamma}_{N_2^+}\frac{S_T}{V_{IR}} - \boldsymbol{\Gamma}_{N_2^+}\frac{(S_{IR}-S_T)(1-\beta_{N_2^+})}{V_{IR}} + \left(k_{iz,\,N_2}n_e + k_{iz,\,N_2}^H n_{e^H}\right)n_{N_2} + \left(k_{iz,\,N_2^m}n_e + k_{iz,\,N_2^m}^H n_{e^H}\right)n_{N_2^m} + k_{N_2-N^+}n_{N_2}n_{N^+} + k_{Ar^+-N_2}n_{Ar^+}n_{N_2}. \quad (A10)$$

(7) $N_2^m$ molecule:


© Author(s) 2025

$$\frac{dn_{N_2^m}}{dt} = -\left(k_{iz,N_2^m}n_e + k^H_{iz,N_2^m}n_{e^H}\right)n_{N_2^m} - k_{N_2^m-N}n_{N_2^m}n_N - k_{N_2^m-N_2}n_{N_2^m}n_{N_2} - k_{dex,N_2^m}n_{N_2^m} - \Gamma_{N_2^m,diff}\frac{S_{IR}-S_T}{V_{IR}} - \Gamma_{Al,coll}\frac{m_{Al}}{m_{N_2^m}}\frac{n_{N_2^m}}{n_{gas}}\frac{S_{IR}-S_T}{V_{IR}} + \left(k_{ex,N_2^m}n_e + k^H_{ex,N_2^m}n_{e^H}\right)n_{N_2}. \quad (A11)$$

(8) N atom:

$$\frac{dn_N}{dt} = -\left(k_{iz,N}n_e + k^H_{iz,N}n_{e^H}\right)n_N - k_{N_2^+-N}n_{N_2^+}n_N - \Gamma_{N,diff}\frac{S_{IR}-S_T}{V_{IR}} - \Gamma_{Al,coll}\frac{m_{Al}}{m_N}\frac{n_N}{n_{gas}}\frac{S_{IR}-S_T}{V_{IR}} + 2k_{diss}n_{N_2}n_e + 2k_{diss2}n_{N_2^+}n_e + k_{N_2-N^+}n_{N_2}n_N + \Gamma^N_{AlN,sput}\frac{S_T}{V_{IR}}, \quad (A12)$$

where $\Gamma^N_{AlN,sput} = \theta\sum\Gamma_{ion}Y^N_{ion,AlN}$ is the sputtering flux of N atoms.

(9) $N^+$ ion:

$$\frac{dn_{N^+}}{dt} = -k_{N_2-N^+}n_{N^+}n_{N_2} - \Gamma_{N^+}\frac{S_T}{V_{IR}} - \Gamma_{N^+}\frac{(S_{IR}-S_T)(1-\beta_{N^+})}{V_{IR}} + (k_{iz,N}n_e + k^H_{iz,N}n_{e^H})n_N + k_{N_2^+-N}n_N n_{N_2^+}. \quad (A13)$$

(10) Al atom:

$$\frac{dn_{Al}}{dt} = -\left(k_{iz,Al}n_e + k^H_{iz,Al}n_{e^H}\right)n_{Al} - k_{chexc}n_{Ar^+}n_{Al} - k_P n_{Ar^m}n_{Al} - \Gamma_{Al,diff}\frac{S_{IR}-S_T}{V_{IR}} + \Gamma_{Al,sput}\frac{S_T}{V_{IR}}, \quad (A14)$$

where $\Gamma_{Al,sput} = (1-\theta)\sum\Gamma_{ion}Y_{ion,Al} + \theta\sum\Gamma_{ion}Y^{Al}_{ion,AlN}$ is the sputtering flux of Al atoms.

(11) $Al^+$ ion:

$$\frac{dn_{Al^+}}{dt} = -\Gamma_{Al^+}\frac{S_T}{V_{IR}} - \Gamma_{Al^+}(1-\beta_{Al^+})\frac{S_{IR}-S_T}{V_{IR}} - (k_{iz,Al^+}n_e + k^H_{iz,Al^+}n_{e^H})n_{Al^+} + (k_{iz,Al}n_e + k^H_{iz,Al}n_{e^H})n_{Al} + k_{chexc}n_{Ar^+}n_{Al} + k_P n_{Ar^m}n_{Al}. \quad (A15)$$

(12) $Al^{2+}$ ion:

$$\frac{dn_{Al^{2+}}}{dt} = (k_{iz,Al^+}n_e + k^H_{iz,Al^+}n_{e^H})n_{Al^+} - \Gamma_{Al^{2+}}\frac{S_T}{V_{IR}} - \Gamma_{Al^{2+}}(1-\beta_{Al^{2+}})\frac{S_{IR}-S_T}{V_{IR}}. \quad (A16)$$

### 2. Particle balance equations of electrons

(1) Cold electron e:

$$\frac{dn_e}{dt} = (k_{iz}n_e + k^H_{iz}n_{e^H})(n_{Ar} + n_{Ar^H}) + (k_{miz}n_e + k^H_{miz}n_{e^H})n_{Ar^m} + (k_{Al,iz}n_e + k^H_{Al,iz}n_{e^H})n_{Al} + (k_{Al^+,iz}n_e + k^H_{Al^+,iz}n_{e^H})n_{Al^+}n_e + (k_{N,iz}n_e + k^H_{N,iz}n_{e^H})n_N + (k_{N_2,iz}n_e + k^H_{N_2,iz}n_{e^H})n_{N_2} + (k_{N_2^m,iz}n_e + k^H_{N_2^m,iz}n_{e^H})n_{N_2^m} + k_P n_{Al}n_{Ar^m} - k_{diss2}n_{N_2^+}n_e - \Gamma_e\frac{S_{IR}-S_T}{V_{IR}}. \quad (A17)$$

The flux of cold electrons $\Gamma_e$ can be calculated as

$$\Gamma_e = D_e\nabla n_{el} + \frac{D_e}{T_e}n_{el}E \approx n_{el}\frac{D_e}{R_{IR}}\left(1+\frac{U_{IR}}{T_e}\right), \quad (A18)$$

where $n_{el} \approx 0.4n_e$ is the electron density on the boundary of the ionization region. $D_e = \frac{1}{\omega\tau}\frac{T_e}{B}$ is the Bohm diffusion coefficient of cold electrons, in which $\omega\tau$ is the ratio of electron cyclotron and collision frequency, and $B$ (T) is the average magnetic field intensity of the target surface.

(2) Hot electron $e^H$:

$$\frac{dn_{e^H}}{dt} = \frac{1}{eU_D/2}\left(\frac{U_{SH}I_{se}}{V_{IR}} - Q^H\right) - \Gamma_{e^H}\frac{S_{IR}-S_T}{V_{IR}}, \quad (A19)$$

where $U_D$ (V) is the discharge voltage and $U_{SH}= U_D- U_{IR}$ is the voltage drop in the sheath. $I_{se}$ (A) is the secondary electron current, as shown as[4]

$$I_{se} = eS_T\left((1-\theta)\sum\Gamma_{ion}\gamma_{ion,Al} + \theta\sum\Gamma_{ion}\gamma_{ion,AlN}\right), \quad (A20)$$

in which $\gamma$ is the secondary electron emission coefficient calculated as

$$\gamma_{ion,target} = 0.016(E_{iz,ion} - 2E_{\varphi,target}),\ \text{target} = \text{Al or AlN}, \quad (A21)$$

where $E_\varphi$ is the electronic work function of target. For Al and AlN, $E_\varphi$ is equal to 4.28 eV (Ref. 25) and 3.7 eV (Ref. 26), respectively.$Q^H$ (W/m$^3$) stands for the energy loss of hot electrons in the inelastic collision with the atoms, as shown as

$$\frac{Q^H}{e} = \sum(E_{j,c} + E_{htc})k^H_{iz,j}n_{e^H}n_j - E_{dex}k^H_{dex}n_{e^H}n_{Ar^m} \quad (A22)$$
$$j = \text{Ar, Ar}^m,\ N_2,\ N_2^m,\ N,\ Al,\ \text{and } Al^+,$$

where $E_{htc} = 10$ eV is the energy loss from hot electron to cold electron. $E_{j,c}$ (eV) can be calculated as follows:

$$k_{iz}E_{Ar,c} = k_{iz}E_{iz} + k_{ex}E_{ex} + k_{el}\frac{3m_e}{m_{Ar}}T_e, \quad (A23)$$

$$k_{miz}E_{Ar^m,c} = k_{miz}E_{miz} + k_{el}\frac{3m_e}{m_{Ar}}T_e, \quad (A24)$$

$$k_{iz,N_2}E_{N_2,c} = k_{iz,N_2}E_{iz,N_2} + k_{ex,N_2}E_{ex,N_2} + k_{el,N_2}\frac{3m_e}{m_{N_2}}T_e, \quad (A25)$$

$$k_{iz,N_2^m}E_{N_2^m,c} = k_{iz,N_2^m}E_{iz,N_2^m} + k_{el,N_2}\frac{3m_e}{m_{N_2}}T_e, \quad (A26)$$

$$k_{iz,N}E_{N,c} = k_{iz,N}E_{iz,N} + k_{el,N}\frac{3m_e}{m_N}T_e, \quad (A27)$$

$$k_{iz,Al}E_{Al,c} = k_{iz,Al}E_{iz,Al} + k_{el,Al}\frac{3m_e}{m_{Al}}T_e, \quad (A28)$$

$$k_{iz,Al^+}E_{Al^+,c} = k_{iz,Al^+}E_{iz,Al^+} + k_{el,Al}\frac{3m_e}{m_{Al}}T_e. \quad (A29)$$

The flux of cold electrons $\Gamma_{e^H}$ can be calculated by[19]

$$\Gamma_{e^H} = \frac{D_{e^H}}{R_{IR}}n_{e^H1}\left(1+\frac{U_{IR}}{T_{e^H}}\right), \quad (A30)$$

where $D_{e^H} = \frac{1}{\omega\tau\sqrt{\frac{T_{e^H}}{T_e}}}\frac{T_{e^H}}{B}$ is the Bohm diffusion coefficient of hot electrons. $T_{e^H}$ is the temperature of the hot electron, as shown as[24]


© Author(s) 2025

$$\mathrm{T}_{\mathrm{e^H}} = \begin{cases} U_{\mathrm{SH}}/3, \ \mathrm{T_e} \le U_{\mathrm{SH}}/3, \\ \mathrm{T_e}, \ \mathrm{T_e} > U_{\mathrm{SH}}/3. \end{cases} \quad \text{(A31)}$$

### 3. Energy balance equation

$$\frac{\mathrm{d}}{\mathrm{d}t}\left(\frac{3}{2}en_e\mathrm{T_e}\right) = F_{\mathrm{PWR}}\frac{P_{\mathrm{D}}}{V_{\mathrm{IR}}} - Q - \left(\frac{3}{2}\mathrm{eT_e}\boldsymbol{\Gamma}_e\frac{S_{\mathrm{IR}} - S_{\mathrm{T}}}{V_{\mathrm{IR}}} + \sum\frac{1}{2}\mathrm{eT_e}\boldsymbol{\Gamma}_{\mathrm{ion}}\frac{S_{\mathrm{T}} + (S_{\mathrm{IR}} - S_{\mathrm{T}})(1-\beta_{\mathrm{ion}})}{V_{\mathrm{IR}}}\right), \quad \text{(A32)}$$

where $P_{\mathrm{D}}$ is the discharge power which could be directly measured by the discharge experiment. $Q$ (W/m$^3$) is the energy variation of collisions between electrons and atoms, as shown as

$$Q = \sum E_{\mathrm{j,c}}k_{\mathrm{iz,j}}n_e n_{\mathrm{j}} + E_{\mathrm{dex}}k_{\mathrm{dex}}n_e n_{\mathrm{Ar^m}} + E_{\mathrm{dex,\,N_2^m}}k_{\mathrm{dex,\,N_2^m}}n_{\mathrm{N_2^m}} + E_{\mathrm{N_2^m-N}}k_{\mathrm{N_2^m-N}}n_{\mathrm{N_2^m}}n_{\mathrm{N}} + E_{\mathrm{N_2^m-N_2}}k_{\mathrm{N_2^m-N_2}}n_{\mathrm{N_2^m}}n_{\mathrm{N_2}} + E_{\mathrm{p}}k_{\mathrm{p}}n_{\mathrm{Al}}n_{\mathrm{Ar^m}}. \quad \text{(A33)}$$

$F_{\mathrm{PWR}}$ is the effective power transfer coefficient (from the power supply to heat the electron), as shown as

$$F_{\mathrm{PWR}} = \frac{\mathrm{e}V_{\mathrm{IR}}E_{\mathrm{htc}}\nu_{\mathrm{iz}}^{\mathrm{H}} + U_{\mathrm{IR}}I_{\mathrm{D}}/2}{U_{\mathrm{D}}I_{\mathrm{D}}}, \quad \text{(A34)}$$

where $I_{\mathrm{D}}$ is the discharge current. Here, $\mathrm{e}V_{\mathrm{IR}}E_{\mathrm{htc}}\nu_{\mathrm{iz}}^{\mathrm{H}}$ is the power input for the heating of second electron, and $U_{\mathrm{IR}}I_{\mathrm{D}}/2$ power input by Ohm heating. $\nu_{\mathrm{iz}}^{\mathrm{H}}$ is the ionization collision of the hot electron with other particles, as shown as

$$\nu_{\mathrm{iz}}^{\mathrm{H}} = n_{\mathrm{e^H}}\left(k_{\mathrm{iz}}^{\mathrm{H}}(n_{\mathrm{Ar}} + n_{\mathrm{Ar^H}}) + k_{\mathrm{iz}}^{\mathrm{H}}n_{\mathrm{Ar^m}} + k_{\mathrm{N_2,\,iz}}^{\mathrm{H}}n_{\mathrm{N_2}} + k_{\mathrm{N_2^m,\,iz}}^{\mathrm{H}}n_{\mathrm{N_2^m}} + k_{\mathrm{N,\,iz}}^{\mathrm{H}}n_{\mathrm{N}} + k_{\mathrm{Al,\,iz}}^{\mathrm{H}}n_{\mathrm{Al}} + k_{\mathrm{Al^+,\,iz}}^{\mathrm{H}}n_{\mathrm{Al^+}}\right). \quad \text{(A35)}$$

### 4. Iterative modification of the erosion profile

The changed parameters during the iterative process are shown in Fig. 10.

### 5. Target poisoning model

Three layers named surface, subsurface, and the bulk, respectively, are always used to describe the target poisoning,[6,21,37] as shown in Fig. 11(a). The $N_2^+$ and $N^+$ sub-plantation takes place only in case 1, which forms case 2 once the $N_2^+$ and $N^+$ arrive the target subsurface. However, case 2 will immediately go into case 3 due to the fast erosion of Al layer at high power density, and into case 4 because of the rapid poisoning at low power density. Therefore, we can ignore case 2 which includes subsurface, but the sub-plantation hasn't been ignored and it is calculated in the reaction from case 1 to case 3 or case 4, as shown in Fig. 11(b).

### 6. Sputtering yield

All the sputtering yield is calculated by TRIM,[38] as shown in Fig. 12.

## REFERENCES


1. C. Saringer, R. Franz, K. Zorn, and C. Mitterer, J. Vac. Sci. Technol. A **34**, 041517 (2016).
2. D. Depla and S. Mahieu, *Reactive Sputter Deposition* (Springer-Verlag, Berlin, Heidelberg, 2008).
3. S. H. Cui, Q. H. Chen, Y. X. Guo, L. Chen, Z. Jin, X. T. Li, C. Yang, Z. C. Wu, X. Y. Su, Z. Y. Ma, R. K. Y. Fu, X. B. Tian, P. K. Chu, and Z. Z. Wu, J. Phys. D: Appl. Phys. **55**, 325203 (2022).
4. D. Depla, K. Strijckmans, and R. De Gryse, Surf. Coat. Technol. **258**, 1011–1015 (2014).
5. F. Perry, A. Billard, and C. Frantz, Surf. Coat. Technol. **94–95**, 339 (1997).
6. B. C. Zheng, Z. L. Wu, B. Wu, Y. G. Li, and M. K. Lei, J. Appl. Phys. **121**, 171901 (2017).
7. S. Berg and T. Nyberg, Thin Solid Films **476**, 215–230 (2005).
8. S. Berg, H. Blom, T. Larsson, and C. Nender, J. Vac. Sci. Technol. A **5**, 202 (1987).
9. S. Berg, T. Larsson, C. Nender, and H. O. Blom, J. Appl. Phys. **63**, 887 (1988).
10. S. Berg and T. Nyberg, Patent No. WO 03/006703A1 (2001).
11. D. Güttler, R. Grötzschel, and W. Möller, Appl. Phys. Lett. **90**, 263502 (2007).
12. D. Güttler, B. Abendroth, R. Grötzschel, W. Möller, and D. Depla, Appl. Phys. Lett. **85**, 6134–6136 (2004).
13. S. H. Cui, L. L. Liu, Z. Jin, L. Zhou, Q. D. Ruan, Z. C. Wu, R. K. Y. Fu, X. B. Tian, P. K. Chu, and Z. Z. Wu, J. Appl. Phys. **129**, 243301 (2021).
14. J. T. Gudmundsson, D. Lundin, and N. Brenning, Plasma Sources Sci. Technol. **25**, 065004 (2016).
15. C. Q. Huo, M. A. Raadu, and D. Lundin, Plasma Sources Sci. Technol. **21**, 045004 (2012).
16. C. Q. Huo, D. Lundin, and M. A. Raadu, Plasma Sources Sci. Technol. **23**, 025017 (2014).
17. A. E. Wendt and M. A. Lieberman, J. Vac. Sci. Technol. A **8**, 902–907 (1990).
18. M. A. Lieberman and A. J. Lichtenberg, *Principles of Plasma Discharges and Materials Processing* (John Wiley and Sons Inc., 2005).
19. L. Chen, S. H. Cui, W. Tang, L. Zhou, T. J. Li, L. L. Liu, X. K. An, Z. C. Wu, Z. Y. Ma, H. Lin, X. B. Tian, K. Y. R. Fu, K. P. Chu, and Z. Z. Wu, Plasma Sources Sci. Technol. **29**, 025016 (2020).
20. T. Kozak and J. Vlcek, J. Phys. D: Appl. Phys. **49**, 055202 (2016).
21. K. Strijckmans and D. Depla, J. Phys. D: Appl. Phys. **47**, 235302 (2014).
22. S. H. Cui, Z. Z. Wu, S. Xiao, B. C. Zheng, L. Chen, T. J. Li, R. K. Y. Fu, P. K. Chu, X. B. Tian, W. C. Tan, D. N. Fang, and F. Pan, J. Appl. Phys. **127**, 023301 (2020).
23. S. M. Rossnagel and H. R. Kaufman, J. Vac. Sci. Technol. A **6**, 223 (1988).
24. C. Huo, D. Lundin, J. T. Gudmundsson, M. A. Raadu, J. W. Bradley, and N. Brenning, J. Phys. D: Appl. Phys. **50**, 354003 (2017).
25. A. Anders, J. Andersson, and A. Ehiasarian, J. Appl. Phys. **102**, 113303 (2007).
26. V. N. Tondare, C. Balasubramanian, S. V. Shende, D. S. Joag, V. P. Godbole, S. V. Bhoraskar, and M. Bhadbhade, Appl. Phys. Lett. **80**, 4813–4815 (2002).
27. J. T. Gudmundsson and E. G. Thorsteinsson, Plasma Sources Sci. Technol. **16**, 399 (2007).
28. M. H. Lee and C. W. Chung, Phys. Plasmas **12**, 073501 (2005).
29. S. Ashida, C. Lee, and M. A. Lieberman, J. Vac. Sci. Technol. A **13**, 2498 (1995).
30. K. Tao, D. Mao, and J. Hopwood, J. Appl. Phys. **91**, 4040 (2002).
31. R. S. Freund, R. C. Wetzel, and R. J. Shul, Phys. Rev. A **41**, 5861 (1990).
32. P. C. Cosby, J. Chem. Phys. **98**, 9544 (1993).
33. E. G. Thorsteinsson and J. T. Gudmundsson, Plasma Sources Sci. Technol. **18**, 045001 (2009).
34. M. A. Lennon, K. L. Bell, H. B. Gilbody, J. G. Hughes, A. E. Kingston, M. A. Murray, and F. J. Smith, J. Phys. Chem. Ref. Data **17**, 1285 (1988).
35. M. A. Raadu, I. Axnäs, J. T. Gudmundsson, C. Huo, and N. Brenning, Plasma Sources Sci. Technol. **20**, 065007 (2011).
36. N. V. Obraztsov, D. I. Subbotin, V. E. Popov, V. Y. Frolov, and A. V. Surov, J. Phys.: Conf. Ser. **1038**, 012137 (2018).
37. T. Kubart, M. Aiempanakit, J. Andersson, T. Nyberg, S. Berg, and U. Helmersson, Surf. Coat. Technol. **205**, S303 (2011).
38. J. F. Ziegler, M. D. Ziegler, and J. P. Biersack, Nucl. Instrum. Methods B **268**, 1818 (2010).



© Author(s) 2025